

# Automated Discovery of Coupled Mode Setups

Jonas Landgraf,<sup>1,2,\*</sup> Vittorio Peano,<sup>1</sup> and Florian Marquardt<sup>1,2</sup>

<sup>1</sup>*Max Planck Institute for the Science of Light, Staudtstr. 2, 91058 Erlangen, Germany*

<sup>2</sup>*Physics Department, University of Erlangen-Nuremberg, Staudtstr. 5, 91058 Erlangen, Germany*

(Dated: April 24, 2024)

In optics and photonics, a small number of building blocks, like resonators, waveguides, arbitrary couplings, and parametric interactions, allow the design of a broad variety of devices and functionalities, distinguished by their scattering properties. These include transducers, amplifiers, and nonreciprocal devices, like isolators or circulators. Usually, the design of such a system is hand-crafted by an experienced scientist in a time-consuming process where it remains uncertain whether the simplest possibility has indeed been found. In our work, we develop a discovery algorithm that automates this challenge. By optimizing the continuous and discrete system properties our automated search identifies the minimal resources required to realize the requested scattering behavior. In the spirit of artificial scientific discovery, it produces a complete list of interpretable solutions and leads to generalizable insights, as we illustrate in several examples. This now opens the door to rapid design in areas like photonic and microwave architectures or optomechanics.

Waves represent one of the most basic physical phenomena. This explains the importance of applications enabled by wave transport in suitably designed structures, ranging from integrated photonics to microwave circuits. A large class of on-chip devices, from isolators and circulators for non-reciprocal transport [1–4] to hybrid frequency converters [5, 6] and new classes of amplifiers [7, 8], can be engineered by combining the right building blocks in a well-chosen scattering topology. So far, each new design in this domain has been proposed based on human ingenuity and experience. It would be desirable to speed up the pace of this laborious exploration process in the high-dimensional space of possible setups and obtain a complete overview of all conceptually distinct options for any given desired functionality. Here, we introduce an automated discovery algorithm that achieves these goals and also helps to uncover new insights.

Tackling challenges of this kind is the domain of artificial scientific discovery [9]. This rapidly evolving field has the ambitious aim to automate all aspects of the scientific process using tools of machine learning and artificial intelligence, with an emphasis on interpretability and discovery of new conceptual insights. Pioneering examples are the identification of organic molecules from mass spectrometry by the computer program Dendral [10] and the generation and experimental testing of hypotheses in biochemistry by a robot scientist [11]. Important challenges in this field include automatic extraction of symbolic expressions [12, 13], discovery of collective coordinates [14, 15], automated planning and execution of experiments [16, 17], and generating new experimental setups. The latter task has been successfully demonstrated for the preparation of multi-photon states in quantum optics [18, 19], for the optimization of superconducting circuits [20], gravitational wave detectors [21], and signal processing using optical components [22].

Automated discovery relies crucially on casting the complex search space into a unifying language. For the domain envisaged here, we identified coupled-mode theory as providing a sweet spot on the continuum between more microscopic hardware-specific descriptions (such as engineered refractive-index distributions [23, 24]) and descriptions based on macroscopic building blocks on the level of entire functional elements (like amplifiers). The latter require a larger number of building blocks and need more human design input. For example [22] focuses on signal processing setups that can be decomposed into directed networks of specific technical components. In contrast, coupled-mode designs are transferable between different platforms and can always be translated back into concrete physical structures. Of equal importance is the formalization of the goal. Here, we chose a description in terms of the scattering matrix, specifying the desired functionality via the externally visible characteristics.

Our discovery algorithm is based on an efficient search process that exploits the recursive modular structure of the problem to prune the exponentially large space of possibilities and provide a complete list of setups fulfilling specified constraints. It automatically ends up with interpretable and generalizable results both by using discrete building blocks and by suggesting only dimensionless parameters of universal, implementation-independent meaning. The final outcome is a menu of irreducible setups that allows to select optimality criteria even afterwards. Moreover, we introduce a fruitful general extension of the toolbox available in artificial discovery, observing that conceptual insights in design are often based on thinking about idealized structures realizing asymptotic limits of parameters. We describe a modification of our algorithm that exploits this meta-principle.

We illustrate the benefits of this approach for a variety of target functionalities, including couplers, circulators and directional amplifiers, where it gives rise to new discoveries and generalizable insights.

We consider a network of coupled bosonic modes,

\* [Jonas.Landgraf@mpl.mpg.de](mailto:Jonas.Landgraf@mpl.mpg.de)

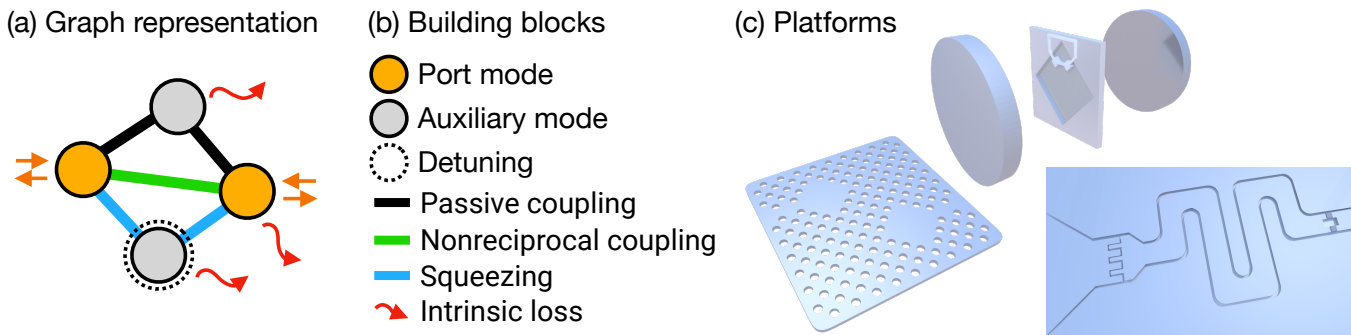


FIG. 1. **Graph representation of coupled mode systems.** (a) Physical modes correspond to graph nodes, couplings to edges. Port modes (orange) are connected to waveguides which relay input and output signals. (b) Discrete building blocks available to the discovery algorithm. (c) Illustration of hardware platforms which are efficiently described by coupled mode theory. This includes photonic crystals (left), optomechanical setups (top), and microwave setups (right).

which can be implemented as an optical, electric, mechanical, or hybrid setup, comprising different types of modes. This device is probed with multiple input signals. We assume that the interaction between the modes can be engineered within some constraints, set by the envisioned experimental implementation. Our method takes into account these constraints but also that certain types of interaction might be more difficult to realize than others, which is factored in the definition of the setup complexity. The choices for the mode and interaction types produce a large discrete search space growing exponentially with the number of modes required for a target response.

The linear response of a multi-mode circuit to signals of a given frequency is encoded in its scattering matrix  $S$ . The element  $S_{ji}$  is the transmission coefficient of a signal from the input port  $i$  to the output port  $j$ . In our work, we aim to automatically discover the simplest setups that fulfill a certain target response, which is encoded in a target scattering matrix  $S_{\text{target}}$ .

The precise characterization of a specific physical implementation of an ideal target device requires a carefully crafted system-specific model. In contrast, the ideal behavior is typically captured by a simple and general high-level description. Like a human scientist would do, we choose our artificial scientist to adopt such high-level description. This approach allows us to discover ideal and transferable solutions.

At the highest level of description, any multi-mode circuit can be represented as a graph with colored edges [25] (see Fig. 1(a,b)), regardless of the underlying hardware platform (see examples in Fig. 1(c)). Nodes correspond to modes and edges correspond to physical interactions. “Port modes” (orange) are connected to waveguides transmitting the input and output signals of interest. We note that the carrier frequencies  $\omega_{L,j}$  of the input fields should be close to the respective mode resonances  $\omega_j$  and can be different for different port modes, e.g. an optical and a mechanical mode will have very different frequencies. We focus on a fixed set of frequencies, but

our approach could be extended to also consider aspects like optimizing the bandwidth [26].

The port modes are often insufficient to implement a given scattering matrix. Therefore, we introduce a variable number of auxiliary modes (grey) interacting with the port modes via the available interactions.

A linear multi-mode scattering setup can contain several interactions: passive coupling (black), nonreciprocal coupling (green) acquiring a direction-dependent phase, and squeezing (blue). It is useful to distinguish between these different types of quadratic interactions because in relevant experimental scenarios, they require qualitatively different implementations. Passive coupling can be realised, e.g. by evanescent coupling between defects modes in a photonic crystal. In contrast, the other interactions are typically generated by pumping a weak higher-order coupling, e.g. using a Kerr medium or optomechanics, or, for nonreciprocal coupling with a directional phase, by coupling modes that are not invariant under the time-reversal symmetry, e.g. whispering gallery modes [27]. In any case, all of these interactions can be written in the form  $g_{ij}\hat{a}_i^\dagger\hat{a}_j + h.c.$  (with  $g_{ij}$  real-valued for passive coupling) or  $\nu_{ij}\hat{a}_i^\dagger\hat{a}_j^\dagger + h.c.$ , respectively (using a rotating wave approximation; see Supplemental Material). Here,  $h.c.$  denotes the Hermitian conjugate, and  $\hat{a}_j^\dagger$  excites mode  $j$ . The coupling rates  $\nu_{ij}$  can be viewed as elements of a symmetric matrix,  $g_{ij}$  as elements of a Hermitian matrix. In our description, any pair of off-diagonal non-zero elements,  $\nu_{ij} \neq 0$  or  $g_{ij} \neq 0$ , corresponds to a graph edge.

To identify setups that implement the target scattering matrix, we have to explore the discrete search space of all possible graphs and, given a graph, find an appropriate set of values for the underlying continuous parameters, i.e., the non-zero couplings, phases, and loss rates. To this end, we perform a two-step procedure: A discrete optimization routine suggests new graphs and an embedded continuous optimization algorithm looks for appropriate values of the parameters (see Fig. 2(a)). If the continuous optimization is successful, we label a graph

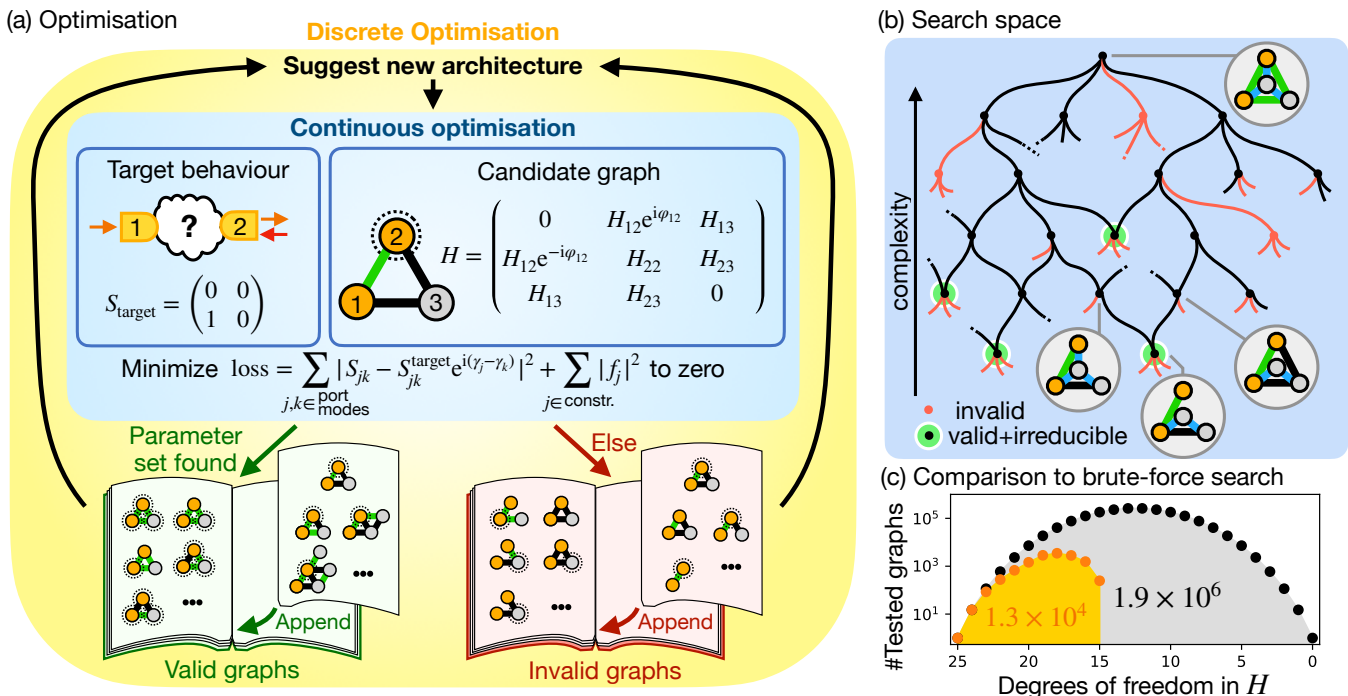


FIG. 2. **Automated Discovery of Modular Scattering Setups.** (a) Optimisation scheme. The discrete optimization sorts graphs into the libraries of valid (green book) and invalid graphs (red book). In every round, a new graph is suggested and, depending on the outcome of the continuous optimisation, sorted with all its extensions/subgraphs into the library of valid/invalid graphs. The continuous optimization minimizes the loss function to realize a target scattering behaviour (left block), here an isolator. The candidate graph (right block) defines the number of auxiliary modes and an allowed set of non-zero couplings rates and phases in the dimensionless Hamiltonian  $H$ . (b) Search space (schematic), starting with a fully connected graph and successively pruning edges, resulting in multiple irreducible solutions. (c) Comparison of the number of tested graphs for the directional coupler (see Fig. 3(b)), which uses five modes. The total number of possible graphs (black) for a certain number of free variables in  $H$  is compared to the number of graphs which had actually to be tested by our exhaustive search. Our scheme starts with maximally connected graphs and successively goes to more restricted graphs. By testing only around 13,000 graphs we are able to characterize all 1.9 million graphs in this example.

as valid.

First, we discuss the discrete optimization, see Fig. 2(a). We aim to identify the simplest valid graphs as they represent the simplest experimental implementations of the target response. Often there exist a multitude of valid graphs that differ in the number and the complexity of the required couplings. Our algorithm identifies “irreducible” graphs that can not be further simplified by setting any coupling rate or phase to zero. To identify all such graphs we perform a complete enumeration.

Due to the large discrete search space, a brute-force approach testing all graphs is infeasible in many cases of interest. We solve this problem by leveraging the knowledge gained from previously tested graphs, drastically reducing the required computational resources. Note that an alternative approach could be developed based purely on continuous optimization, introducing terms in a loss function that reward sparsity (zero couplings) as in [28–30] – however, this would not enable us to obtain a complete set of solutions.

We take advantage of the fact that removing an edge from a graph is equivalent to setting a coupling rate to

zero. Thus, if a graph is found to be invalid, that carries over to all graphs which can be generated by removing some edges and/or setting coupling phases to zero (changing an edge color from green to black). Likewise, all extensions of a valid graph are valid (see Fig. 2(b)). This observation allows us to efficiently construct exhaustive libraries of valid and invalid graphs by testing only a small fraction, see Fig. 2(c).

First, we test only fully connected graphs for validity, until we identify the minimum required number of modes. Starting from that parent graph, our algorithm suggests at every iteration a new graph that is not yet included in any of the two libraries and tests for validity. If no solution is discovered by the continuous optimization, the graph and all its subgraphs are added to the library of invalid graphs. Otherwise, the graph and all its extensions are added to the library of valid graphs. If some of the discovered parameters turn out to be zero, the corresponding simpler graph and all its extensions are added instead.

We now turn to the continuous optimization. The scattering matrix  $S$  is fully determined by an appropriately

defined first-quantized dimensionless Hamiltonian  $H$  (see below), which contains the free coupling parameters. We look for setups implementing the desired scattering behavior by minimizing the square deviation loss function with respect to those couplings:

$$\mathcal{L} = \sum_{j,k \in \text{port modes}} \left| S_{jk} - S_{jk}^{\text{target}} e^{i(\gamma_j^{\text{out}} - \gamma_k^{\text{in}})} \right|^2 + \sum_{j \in \text{constr.}} |f_j|^2. \quad (1)$$

We note that the target scattering matrix  $S^{\text{target}}$  can contain further free parameters that are not specified by the desired scattering properties. For example, we might impose that two scattering amplitudes are equal but a suitable value needs to be discovered. In addition, we introduce the free parameters  $\gamma_i^{\text{in/out}}$  to account for the fact that the optical path length of the input and output fields in the waveguide can be easily modified. Finally, we allow for extra constraints  $f_j$  that can be expressed in terms of the multi-mode circuit parameters or the scattering matrix  $S$ , e.g. when enforcing minimum added noise. We minimize the loss  $\mathcal{L}$  as a function of the free parameters in  $H$ ,  $S^{\text{target}}$ , and the phases  $\gamma_i^{\text{in/out}}$ . For the minimization, we use the Broyden–Fletcher–Goldfarb–Shanno algorithm [31], an iterative gradient-descent method for solving non-linear optimization problems. A valid solution is obtained whenever the loss reaches zero. The algorithm fails to find a solution if the loss gets stuck in a non-zero minimum. Since the optimization landscape supports local minima, there is a risk of false-negative errors. To reduce this risk, we repeat the continuous optimization  $N_{\text{rep}}$  times. The hyperparameter  $N_{\text{rep}}$  is chosen empirically.

A key step of our method is to derive the scattering matrix  $S$  in terms of an appropriately rescaled Bogoliubov-de-Gennes Hamiltonian:

$$H = \frac{1}{\sqrt{\kappa}} \begin{pmatrix} g & \nu \\ \nu^* & g^* \end{pmatrix} \frac{1}{\sqrt{\kappa}}, \quad (2)$$

see Supplemental Material. Here,  $\kappa$  is the diagonal matrix  $\kappa = \text{diag}(\kappa_1, \dots, \kappa_N, \kappa_1, \dots, \kappa_N)$  with  $\kappa_i$  being the out-coupling of mode  $i$  into the corresponding output port (for an auxiliary mode it could be an intrinsic loss channel). The rescaling in Eq. (2) is important, since it means the algorithm discovers classes of solutions that depend only on the dimensionless detuning  $-H_{ii} = (\omega_{L,i} - \omega_i)/\kappa_i$ , the cooperativities  $\mathcal{C}_{ij} = 4|H_{ij}|^2$ , and the gauge invariant phases accumulated on closed loops (synthetic field fluxes),  $\Phi_{i,j,l,\dots,k} = \arg(H_{ij}H_{jl} \dots H_{ki})$ . When translating back to a concrete physical setup, this leaves the freedom to choose arbitrarily the decay rates  $\kappa_i$  and thus the couplings (although for amplifiers some additional stability constraints might apply, see Supplemental Material). For simplicity, we focus below on the important special case of phase-preserving devices. In this scenario, the scattering matrix is an  $N \times N$  matrix as already implicitly assumed in Eq. (1). In addition, we have assumed that each port mode is coupled in reflection to a single waveguide. For further details like the

treatment of quantum noise, phase-sensitive amplifiers, coupling in transmission, and application to setups with chiral modes, see the Supplemental Material.

In the following, we demonstrate the successful application of our method to a selected number of illustrative examples.

As a first proof of concept, we apply our scheme to implement an isolator, i.e. a two-port device with perfect transmission from the input to the output and zero reverse transmission, see Fig. 3(a). Our method shows that the simplest solution involves a single auxiliary mode and a single complex coupling. The continuous optimization routine provides also the cooperativities  $\mathcal{C}_{12} = \mathcal{C}_{23} = \mathcal{C}_{31} = 1$  and the synthetic flux  $\Phi_{123} = \pi/2$ , recovering the solution used in [2, 25, 32–34]. In the special limiting case of an overdamped auxiliary mode,  $\kappa_3 \gg \kappa_1, \kappa_2$ , this mode acts as a Markovian bath mediating a dissipative interaction [35]. By adiabatic elimination, one can derive a generalization of the dissipative isolator discussed in [35], see Supplemental Material. It is always possible to translate the solutions discovered by our algorithm into schemes in the spirit of Ref. [35], with an engineered reservoir replacing the auxiliary modes. A closed formula for the corresponding Lindblad Master equation is given in the Supplemental Material.

The aim of artificial scientific discovery is to create generalizable insights. We now demonstrate that the solutions systematically discovered using our scheme can inspire the discovery of more complex devices, e.g. involving an arbitrarily large number of ports. As an example, we consider a fully directional coupler. This is a device that combines signals from multiple input ports and transmits them with equal transmission amplitude to an output port. Here, we aim for a fully directional coupler with zero reflection and reverse-transmission amplitudes, cf Fig. 3(b). We leave the transmission amplitude  $t$  as a free parameter.

First, we use our scheme to find possible solutions for  $N_{\text{in}} = 2$ . It turns out that at least two auxiliary modes are required to realize a two-port device. In total, we find 100 different irreducible graphs that differ in the number and complexity of the underlying couplings. We select the graphs with the minimal number of couplings, Graph (I) with six couplings, and the graphs with the smallest number of non-reciprocal couplings, Graph (II) and (III), requiring seven couplings but only one parametric drive. The remaining irreducible graphs are either gauge transformations of these graphs or require more resources in terms of couplings and parametric drives.

This scenario is an example where the automated discovery process has produced solutions that lead to generalizable insights, an important goal in artificial scientific discovery. Indeed, inspecting Graph (I), we note that it can be viewed as the combination of two isolator graphs. This inspires a general ansatz for an  $N_{\text{in}}$ -port coupler: a graph that comprises an isolator building block for each input port, see the right panel in Fig. 3(b). We then use our continuous optimization routine to verify the valid-

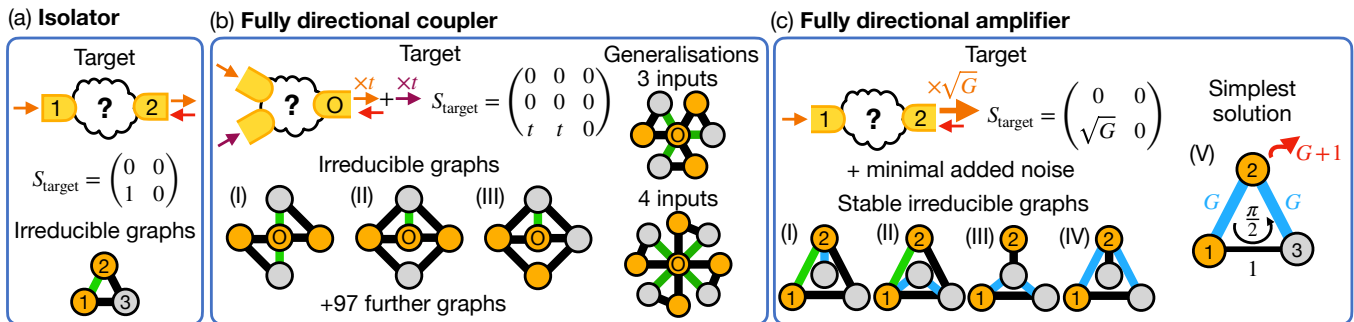


FIG. 3. **Illustrative examples for automated discovery of scattering setups.** Target scattering behaviours and the corresponding irreducible graphs identified by our automated search. (a) Isolator. Only signal from mode 1 to 2 is transmitted. (b) Directional coupler. Multiple input signals are summed up and transmitted to the output port. Graph (I-III) are the smallest irreducible graphs for a directional coupler with two inputs. Graph (I) has the smallest number of couplings, graph (II) and (III) have the smallest number of parametric drives. The other identified 97 further irreducible graphs (not shown) require either more resources or are gauge transformations of the shown graphs. Graph (I) can be generalized to more inputs. (c) Directional amplifier. Input from port 1 is amplified by a factor of  $\sqrt{G}$ , the other direction is blocked. The device has minimal back-action and the noise is quantum-limited. The graphs (I-IV) are the simplest solution without making use of intrinsic loss on the port modes. Allowing intrinsic losses, graph (V) is the simplest graph. Analytical terms discovered for the cooperativities  $\mathcal{C}_{ij}$ , the intrinsic loss rescaled by the outcoupling (red arrow), and the flux  $\Phi_{132}$  are indicated. All shown graphs are stable. The unstable solutions are further discussed in the Supplemental Material.

ity of the ansatz and calculate cooperativities, fluxes, and the transmission  $t$  for the first few  $N_{\text{in}}$ , up to  $N_{\text{in}} = 5$  corresponding to  $N = 11$  nodes. We note that for such large graphs, an exhaustive search of the graph space would be daunting. From the special solutions, we infer a general solution valid for arbitrary  $N_{\text{in}}$ : All cooperativities between an input-port mode and the corresponding auxiliary mode take the same value,  $\mathcal{C}_{\text{in,aux}} = 1$ , the cooperativities between the output-port mode and the other modes take the value  $\mathcal{C}_{\text{out,in/aux}} = 1/N_{\text{in}}$ , and the synthetic field fluxes are the same for all isolator-like loops,  $\Phi_{\text{in,out,aux}} = \pi/2$ . Finally the transmission turns out to be  $t = 1/\sqrt{N_{\text{in}}}$ , implying that no noise from the auxiliary modes is injected into the output port.

In many interesting problems, one might be trying to solve a whole class of tasks where one or several parameters in the target scattering matrix are allowed to vary continuously. This type of challenge can be solved using our algorithm by first identifying a valid graph using a fixed value of the parameter, then using continuous optimization to create a dataset of solutions for varying parameter values (but fixed graph structure), and finally attempting to derive closed analytical formulas for the cooperativities and fluxes by symbolic regression.

To illustrate this, consider several recent works [2, 34–38] that have proposed schemes to realize on-chip directional quantum-limited amplifiers using multi-mode circuits and to replace bulky state-of-the-art ferrite-based devices. The target device has arbitrary gain  $G$  and is fully directional, i. e. has zero back-reflection, and zero reverse-transmission, cf Fig. 3(c). Moreover, both at the input and the output ports the added noise should reach the so-called quantum limit, i.e. the fundamental limit set by the laws of quantum mechanics [39]. The latter

requirements can be translated into constraints on the scattering matrix  $S$  that depend on the temperatures of the input and output ports. For both input and output ports at zero-temperature we recover the solution used in [2, 25, 34, 35]. In this solution, the added noise in the output port is injected into the multi-mode system from the same port. An interesting open problem in this context is to find the simplest design for a fully directional amplifier that is still quantum-limited in the presence of a hot output port [38]. Liu et. al. [38] approached this problem with a hand-crafted approach, discovering two small architectures comprising two auxiliary modes and six couplings. However, applying our method we discovered several smaller architectures, see Fig. 3(c). For more details of our derivations and results, please see the Supplemental Material. The smallest solution comprises a single auxiliary mode, three couplings, and has an under-coupled output port, i. e. most of the signal is dissipated into a (zero-temperature) loss channel. While this setup is not power-efficient, it fulfills all the imposed goals and represents an instructive counter-intuitive solution, since one could naively expect that the loss of a large part of the signal would be incompatible with quantum-limited amplification.

In many physical systems, an ideal target behavior can be reached only in the special limiting case of one or more system parameters that tend to infinity or zero, e.g. a strong coupling limit. Even though this ideal limit is strictly unattainable in practice, adopting it promotes simplification and conceptual understanding. How can we introduce such fruitful asymptotic analysis in the context of artificial scientific discovery? One key complication is that often multiple dimensionless coupling parameters  $\mathcal{C}_j$  need to become infinite simultaneously. This is

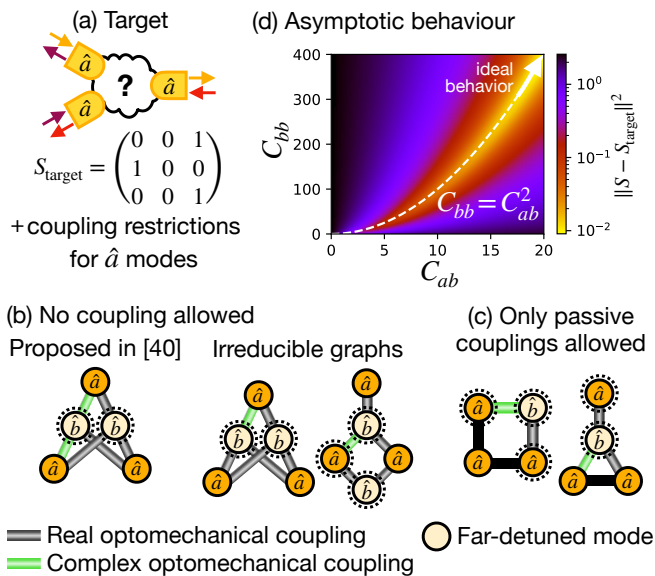


FIG. 4. **Optomechanical circulator.** (a) Target operation: Realize a circulator between optical modes ( $\hat{a}$ ) by mediating the interaction using mechanical modes ( $\hat{b}$ ). (b) No couplings allowed between optical modes: Architecture proposed in [40] (left) and irreducible graphs identified by our scheme (right). Two mechanical modes ( $\hat{b}$ ) mediate the interaction between the optical modes ( $\hat{a}$ ). (c) Irreducible graphs identified by our optimisation scheme if direct passive couplings between the scattering matrix and the target behavior are allowed. (d) Deviation between the scattering matrix and the target behavior for the left graph in (c). The deviation approaches 0 in the asymptotic limit of  $C_{ab}, C_{bb} \rightarrow \infty$  with  $C_{ab}^2/C_{bb} = 1$  (dashed white line).

resolved by rephrasing the description in terms of ratios like  $C_j/C_k$  (or even, more generally,  $C_j^\alpha/C_k$ , with a suitable exponent, depending on the situation). This ratio stays finite while  $C_j, C_k \rightarrow \infty$ , and its numerical value can be found by the discovery algorithm. At the same time, the limit itself can be represented as an idealized building block.

Coming back to the discovery of scattering setups, a generic example of such a building block is a far-detuned bus mode which mediates purely coherent interactions between other modes. Both the bus-mode detuning  $\Delta^{(b)}$  and the couplings to the neighboring modes  $a$  tend to infinity. However, the ratios  $C_{ab}^2/C_{bb} = |g_{ab}|^4/(\kappa_a \Delta^{(b)})^2$  stay finite, and it is these ratios that determine the scattering matrix after integrating out the bus mode. We can thus incorporate the far-detuned mode by adding these ratios as optimization parameters and incorporating the interaction they mediate into the Hamiltonian for the remaining modes (see Supplemental Material). When eventually translating back to a physical setup, we can

freely choose the absolute value of the bus-mode detuning with the only constraint that it is much larger than the corresponding decay rate  $\kappa_b$ . There are plenty of physical examples where such a reasoning is useful, see e.g. [5, 6, 36, 40].

We apply this extended optimization scheme to discover the simplest setup to implement an optomechanical circulator in the experimental scenario considered in [40]. Three microwave port modes are coupled via the optomechanical interactions mediated by a varying number of mechanical modes. No direct coupling is available (see Fig. 4(a)). Since each optomechanical coupling requires a different laser drive, the key measure of experimental complexity in this case is the overall number of couplings. The hand-crafted architecture proposed in [40] requires two far-detuned mechanical modes and six couplings. Our optimization scheme finds a simpler setup, which requires the same number of far-detuned modes but only five couplings (see Fig. 4(b)). If we apply the softer constraint where passive couplings are allowed between the optical modes, our scheme identifies even simpler graphs, only involving one mechanical mode (see Fig. 4(c)). To reach the ideal behaviour, e.g. , for the left graph in Fig. 4(c), the cooperativities  $C_{ab}$  and  $C_{bb}$  have to tend towards infinity, while obeying that the ratio  $C_{ab}^2/C_{bb}$  equals 1 (see Fig. 4(d)).

In conclusion, we have presented an automated-discovery approach that finds irreducible scattering setups, leading to results that provide new insights and are interpretable and generalizable. The approach is amenable to numerous future extensions like search for optimized implementations in specific hardware platforms neural-network-guided heuristics for larger devices where complete enumeration is infeasible, or target specific quantum noise characteristics. More generally, our results now open the door towards automated discovery in additional related domains of high importance, like transport through periodic structures composed of small modular blocks or scattering-based sensing experiments. Nonlinear setups or even devices with functionalities based on time-dependent control require significant new developments, but still could be treated with the same graph-based efficient search algorithm. Overall, we feel that the results shown here validate the fruitfulness of the main ideas guiding the field of artificial scientific discovery.

## ACKNOWLEDGMENTS

We acknowledge fruitful discussions with Mario Krenn, Clara Wanjura, and Flore Kunst.

[1] A. Kamal, J. Clarke, and M. H. Devoret, *Nature Physics* **7**, 311 (2011).

[2] K. M. Sliwa, M. Hatridge, A. Narla, S. Shankar, L. Frun-

- zio, R. J. Schoelkopf, and M. H. Devoret, *Physical Review X* **5**, 041020 (2015).
- [3] G. A. Peterson, F. Lecocq, K. Cicak, R. W. Simmonds, J. Aumentado, and J. D. Teufel, *Physical Review X* **7**, 031001 (2017).
- [4] J. F. Herrmann, V. Ansari, J. Wang, J. D. Witmer, S. Fan, and A. H. Safavi-Naeini, *Nature Photonics* **16**, 603 (2022).
- [5] R. W. Andrews, R. W. Peterson, T. P. Purdy, K. Cicak, R. W. Simmonds, C. A. Regal, and K. W. Lehnert, *Nature Physics* **10**, 321 (2014).
- [6] J. T. Hill, A. H. Safavi-Naeini, J. Chan, and O. Painter, *Nature Communications* **3**, 1196 (2012).
- [7] C. Macklin, K. O'Brien, D. Hover, M. E. Schwartz, V. Bolkhovskiy, X. Zhang, W. D. Oliver, and I. Siddiqi, *Science* **350**, 307 (2015).
- [8] K. Fang, J. Luo, A. Metelmann, M. H. Matheny, F. Marquardt, A. A. Clerk, and O. Painter, *Nature Physics* **13**, 465 (2017).
- [9] H. Wang, T. Fu, Y. Du, W. Gao, K. Huang, Z. Liu, P. Chandak, S. Liu, P. Van Katwyk, A. Deac, *et al.*, *Nature* **620**, 47 (2023).
- [10] R. K. Lindsay, B. G. Buchanan, E. A. Feigenbaum, and J. Lederberg, *Artificial Intelligence* **61**, 209 (1993).
- [11] R. D. King, K. E. Whelan, F. M. Jones, P. G. K. Reiser, C. H. Bryant, S. H. Muggleton, D. B. Kell, and S. G. Oliver, *Nature* **427**, 247 (2004).
- [12] M. Schmidt and H. Lipson, *Science* **324**, 81 (2009).
- [13] S.-M. Udrescu and M. Tegmark, *Science Advances* **6**, 16 (2020).
- [14] R. Iten, T. Metger, H. Wilming, L. del Rio, and R. Renner, *Physical Review Letters* **124**, 010508 (2020).
- [15] L. Sarra, A. Aiello, and F. Marquardt, *Physical Review Letters* **126**, 200601 (2021).
- [16] D. T. Lennon, H. Moon, L. C. Camenzind, L. Yu, D. M. Zumbühl, G. A. D. Briggs, M. A. Osborne, E. A. Laird, and N. Ares, *npj Quantum Information* **5**, 79 (2019).
- [17] J. Duris, D. Kennedy, A. Hanuka, J. Shtalenkova, A. Edelen, P. Baxevanis, A. Egger, T. Cope, M. McIntire, S. Ermon, *et al.*, *Physical Review Letters* **124**, 124801 (2020).
- [18] M. Krenn, M. Malik, R. Fickler, R. Lapkiewicz, and A. Zeilinger, *Physical Review Letters* **116**, 090405 (2016).
- [19] M. Krenn, M. Erhard, and A. Zeilinger, *Nature Reviews Physics* **2**, 649 (2020).
- [20] T. Menke, F. Häse, S. Gustavsson, A. J. Kerman, W. D. Oliver, and A. Aspuru-Guzik, *npj Quantum Information* **7**, 49 (2021).
- [21] M. Krenn, Y. Drori, and R. X. Adhikari, *arXiv:2312.04258* (2023).
- [22] B. MacLellan, P. Roztocky, J. Belleville, L. Romero Cortés, K. Ruscitti, B. Fischer, J. Azaña, and R. Morandotti, *Laser & Photonics Reviews* **2024**, 2300500 (2024).
- [23] A. Y. Piggott, J. Lu, K. G. Lagoudakis, J. Petykiewicz, T. M. Babinec, and J. Vuckovic, *Nature Photonics* **9**, 374 (2015).
- [24] S. Molesky, Z. Lin, A. Y. Piggott, W. Jin, J. Vuckovic, and A. W. Rodriguez, *Nature Photonics* **12**, 659 (2018).
- [25] L. Ranzani and J. Aumentado, *New Journal of Physics* **17**, 023024 (2015).
- [26] O. Naaman and J. Aumentado, *PRX Quantum* **3**, 020201 (2022).
- [27] M. Hafezi, E. A. Demler, M. D. Lukin, and J. M. Taylor, *Nature Physics* **7**, 907 (2011).
- [28] M. Krenn, J. S. Kottmann, N. Tischler, and A. Aspuru-Guzik, *Physical Review X* **11**, 031044 (2021).
- [29] C. Ruiz-Gonzalez, S. Arlt, J. Petermann, S. Sayyad, T. Jaouni, E. Karimi, N. Tischler, X. Gu, and M. Krenn, *arXiv:2210.09980* (2022).
- [30] S. Arlt, C. Ruiz-Gonzalez, and M. Krenn, *arXiv:2210.09981* (2022).
- [31] J. Nocedal and S. J. Wright, *Numerical Optimization*, 2nd ed. (Springer, New York, NY, USA, 2006).
- [32] J. Koch, A. A. Houck, K. L. Hur, and S. M. Girvin, *Physical Review A* **82**, 043811 (2010).
- [33] S. J. M. Habraken, K. Stannigel, M. D. Lukin, P. Zoller, and P. Rabl, *New Journal of Physics* **14**, 115004 (2012).
- [34] F. Lecocq, L. Ranzani, G. A. Peterson, K. Cicak, R. W. Simmonds, J. D. Teufel, and J. Aumentado, *Physical Review Applied* **7**, 024028 (2017).
- [35] A. Metelmann and A. A. Clerk, *Physical Review X* **5**, 021025 (2015).
- [36] D. Malz, L. D. Tóth, N. R. Bernier, A. K. Feofanov, T. J. Kippenberg, and A. Nunnenkamp, *Physical Review Letters* **120**, 023601 (2018).
- [37] B. Abdo, K. Sliwa, L. Frunzio, and M. Devoret, *Physical Review X* **3**, 031001 (2013).
- [38] G. Liu, A. Lingenfelter, V. R. Joshi, N. E. Frattini, V. V. Sivak, S. Shankar, and M. H. Devoret, *Phys. Rev. Appl.* **21**, 014021 (2024).
- [39] A. A. Clerk, M. H. Devoret, S. M. Girvin, F. Marquardt, and R. J. Schoelkopf, *Reviews of Modern Physics* **82**, 1155 (2010).
- [40] N. R. Bernier, L. D. Tóth, A. Koottandavida, M. A. Ioannou, D. Malz, A. Nunnenkamp, A. K. Feofanov, and T. J. Kippenberg, *Nature Communications* **8**, 604 (2017).
- [41] M. Hafezi and P. Rabl, *Optics Express* **20**, 7672 (2012).
- [42] J. Kim, M. C. Kuzyk, K. Han, H. Wang, and G. Bahl, *Nature Physics* **11**, 275 (2015).
- [43] F. Ruesink, M.-A. Miri, A. Alù, and E. Verhagen, *Nature Communications* **7**, 13662 (2016).
- [44] Z. Shen, Y.-L. Zhang, Y. Chen, C.-L. Zou, Y.-F. Xiao, X.-B. Zou, F.-W. Sun, G.-C. Guo, and C.-H. Dong, *Nature Photonics* **10**, 657 (2016).

## Appendix A: Details on the high-level description of a multi-mode circuit

Here, we give more details on our high-level description of multi-mode circuits. For completeness, we consider the most general scenario which encompasses purely-routing devices as well as phase-preserving, and phase-sensitive amplifiers.

### 1. Bogoliubov de Gennes Hamiltonian and the rotating wave approximation

We consider a hybrid system comprising  $N$  modes of different types and the most general quadratic time-independent Hamiltonian

$$\hat{H} = \frac{1}{2} \sum_{j,k=1}^N \left( g_{jk} \hat{a}_j^\dagger \hat{a}_k + \nu_{jk} \hat{a}_j^\dagger \hat{a}_k^\dagger \right) + \text{H.c.} \quad (\text{A1})$$

Here,  $\hat{a}_j$  and  $\hat{a}_j^\dagger$  are the ladder operators of mode  $j$ ,  $g$  is a Hermitian matrix, and  $\nu$  can be chosen to be symmetric. For a more compact notation, it is convenient to group all the modes in a  $2N$  dimensional vector,  $\hat{\xi} = \{\hat{a}_1, \dots, \hat{a}_N, \hat{a}_1^\dagger, \dots, \hat{a}_N^\dagger\}$ , and to introduce the first-quantized Bogoliubov de Gennes Hamiltonian

$$\hat{H} = \frac{1}{2} \hat{\xi}^\dagger H_{\text{BdG}} \hat{\xi}, \quad H_{\text{BdG}} = \begin{pmatrix} g & \nu \\ \nu^* & g^* \end{pmatrix}. \quad (\text{A2})$$

The Hamiltonian Eq. (A1) is defined in a frame in which the phase space of each mode  $j$  rotates at the corresponding carrier frequency  $\omega_{L,j}$ . Thus,  $-g_{jj}$  is to be interpreted as the detuning  $\Delta_j$  of the carrier frequency  $\omega_{L,j}$  from the mode resonance  $\omega_j$ ,  $\Delta_j = \omega_{L,j} - \omega_j$ . For multi-mode circuits, such time-independent Hamiltonian is typically referred to as the rotating-wave Hamiltonian as it is obtained after a Rotating-Wave Approximation (RWA) that drops the fast-oscillating terms, which result from non-resonant interactions. The corrections to the RWA approximation are small if all resonant frequencies  $\omega_j$  are much larger than the coupling rates  $g_{ij}$  and  $\nu_{ij}$  as well as the decay rates  $\kappa_j$ . We note that if all couplings are active the carrier frequencies  $\omega_{L,j}$  for the different modes can be chosen independently of each other, as long as the frequencies of the lasers mediating the interactions are adjusted accordingly. Alternatively, one can use this freedom to choose independently the values of the detunings  $\Delta_j$  in experimental scenarios in which the mode resonances  $\omega_j$  are not tunable. We note that all modes connected by passive coupling have the same carrier frequency which in turn leads to constraints to  $\Delta_j$  for fixed  $\omega_j$ . Besides these constraints, the mode resonances  $\omega_j$  are irrelevant in the high-level description based on the RWA. This is an appealing feature that makes any insight gained using our method highly transferable within a variety of platforms. A more refined description including non-resonant interactions is typically used to quantify how a specific implementation deviates from the ideal target behavior. This deviation is device-specific and, thus, goes beyond the scope of our work.

### 2. Langevin Equations

We use input-output theory to describe the dynamics of the open multi-mode circuit. As described in the main text, we distinguish between port modes, which are used as input and output ports for the signals, and auxiliary ports, which are not used as input ports and whose output is not monitored. Accordingly, all the losses in an auxiliary mode can be incorporated into a single loss channel. On the other hand, whenever we want to incorporate intrinsic losses in the port modes we have to introduce two loss channels for these modes, an out-coupling and an intrinsic loss channel. Based on these considerations, we arrive at the Langevin equations

$$\dot{\hat{a}}_j(t) = -i \sum_k g_{jk} \hat{a}_k(t) - i \sum_k \nu_{jk} \hat{a}_k^\dagger(t) - \frac{\kappa_j + \Gamma_j}{2} \hat{a}_j(t) - \sqrt{\kappa_j} \hat{a}_j^{\text{in}}(t) - \sqrt{\Gamma_j} \hat{a}_j^{\text{noise}}(t) \quad (\text{A3})$$

Here,  $\hat{a}_j^{\text{in}}$  is the input field for the main decay channel (for the port modes the out-coupling channel), with decay rate  $\kappa_j$ . Likewise,  $\hat{a}_j^{\text{noise}}$  is the noise entering a port mode  $j$  from its intrinsic loss channel, which has decay rate  $\Gamma_j$ . The Langevin equations can be rewritten in a compact form as

$$\dot{\hat{\xi}}(t) = \left( -i\sigma_z H_{\text{BdG}} - \frac{\kappa + \Gamma}{2} \right) \hat{\xi}(t) - \sqrt{\kappa} \hat{\xi}^{\text{in}}(t) - \sqrt{\Gamma} \hat{\xi}^{\text{noise}}(t) \quad (\text{A4})$$



Here, we have grouped all input and noise fields in the vectors,  $\hat{\xi}^{\text{in}} = \{\hat{a}_1^{\text{in}}, \dots, \hat{a}_N^{\text{in}}, \hat{a}_1^{\text{in}\dagger}, \dots, \hat{a}_N^{\text{in}\dagger}\}$  and  $\hat{\xi}^{\text{noise}} = \{\hat{a}_1^{\text{noise}}, \dots, \hat{a}_N^{\text{noise}}, \hat{a}_1^{\text{noise}\dagger}, \dots, \hat{a}_N^{\text{noise}\dagger}\}$ , respectively. Moreover, we have introduced the diagonal matrices  $\kappa = \text{diag}(\kappa_1, \dots, \kappa_N, \kappa_1, \dots, \kappa_N)$ ,  $\Gamma = \text{diag}(\Gamma_1, \dots, \Gamma_N, \Gamma_1, \dots, \Gamma_N)$  and

$$\sigma_z = \begin{pmatrix} \mathbb{1}_N & 0 \\ 0 & -\mathbb{1}_N \end{pmatrix}. \quad (\text{A5})$$

We note that the Langevin equations have the embedded particle-hole symmetry  $\sigma_x \mathcal{K}$  where  $\mathcal{K}$  denotes the complex conjugation and

$$\sigma_x = \begin{pmatrix} 0 & \mathbb{1}_N \\ \mathbb{1}_N & 0 \end{pmatrix}. \quad (\text{A6})$$

This simply reflect that the last  $N$  equations are the adjoint of the first  $N$  equations.

### 3. Scattering matrix

To fully characterize the linear response of a multi-mode circuit, one has to take into account that it depends on the frequency of the input field via the time-derivative in the left-hand side of Eq. (A4). However, the ideal scattering behavior is only realized in a high-level description that focuses on signals that have a very smooth envelope and, thus, are spectrally well localized (in each port about the respective carrier frequency  $\omega_j^s$ ). Taking into account that in the rotating frame the frequency is counted off from the respective carrier frequency  $\omega_j^s$ , the response of interest is the “zero-frequency” response obtained by setting  $\dot{\hat{\xi}}(t) = 0$  in Eq. (A4). After calculating  $\hat{\xi}$  in this way and plugging it into the input-output relations

$$\hat{\xi}^{\text{out}} = \hat{\xi}^{\text{in}} + \sqrt{\kappa} \hat{\xi}, \quad (\text{A7})$$

we find

$$\hat{\xi}^{\text{out}} = \underbrace{\left[ \mathbb{1} + \sqrt{\kappa} \left( -i\sigma_z H_{\text{BdG}} - \frac{\kappa + \Gamma}{2} \right)^{-1} \sqrt{\kappa} \right]}_{\text{scattering matrix } S} \hat{\xi}^{\text{in}} \quad (\text{A8a})$$

$$+ \underbrace{\left[ \sqrt{\kappa} \left( -i\sigma_z H_{\text{BdG}} - \frac{\kappa + \Gamma}{2} \right)^{-1} \sqrt{\Gamma} \right]}_{\text{noise matrix } N} \hat{\xi}^{\text{noise}}. \quad (\text{A8b})$$

Here,  $S$  is the scattering matrix and the matrix  $N$  describes the linear response to the fluctuations entering the circuit from the intrinsic loss channels.

In view of discovering classes of solutions displaying the same scattering behavior, we found that it is possible to eliminate the explicit dependence of  $S$  and  $N$  on the decay rates  $\kappa_i$  by appropriately rescaling the Bogoliubov de Gennes Hamiltonian and the intrinsic losses. In particular, we find

$$S = \mathbb{1}_{2N} + \left( -i\sigma_z H - \frac{\gamma}{2} - \frac{\mathbb{1}_{2N}}{2} \right)^{-1} \quad (\text{A9a})$$

$$N = (S - \mathbb{1}_{2N}) \sqrt{\gamma}. \quad (\text{A9b})$$

with

$$H = \frac{1}{\sqrt{\kappa}} H_{\text{BdG}} \frac{1}{\sqrt{\kappa}}, \quad \gamma = \Gamma \kappa^{-1}. \quad (\text{A10})$$

We note that the rescaled Bogoliubov Hamiltonian  $H$  is parametrized by  $N$  rescaled detunings  $H_{ii} = -\Delta_i/\kappa_i$  with  $1 \leq i \leq N$ ,  $N(N-1)/2$  dimensionless couplings  $g_{ij}/\sqrt{\kappa_j \kappa_i}$  with  $1 \leq i < j \leq N$ , and  $N(N+1)/2$  squeezing amplitudes  $\nu_{ij}/\sqrt{\kappa_j \kappa_i}$  with  $1 \leq i \leq j \leq N$ . These parameters are learning parameters in the continuous optimization. As pointed out in the main text, the functionality of the device to depends only on dimensionless detunings  $H_{ii}$ , cooperativities  $\mathcal{C}_{ij} = 4|H_{ij}|^2$ , and the gauge-invariant geometrical phases accumulated on closed loops (synthetic field

fluxes),  $\Phi_{i,j,l,\dots,k} = \arg(H_{ij}H_{jl}\dots H_{ki})$ , see Eq. (A9a). If we allow for intrinsic loss channels in the port modes, the behaviour is furthermore influenced by the dimensionless intrinsic loss rates  $\gamma$ , see Eqs. (A9a) and (A9b).

We note that in the most general case, the  $S$  matrix is a  $2N \times 2N$  matrix, cf Eqs. (A2), (A10) and (A9a). This dimensionality reflects the fact that the intensity of the transmitted field can depend on the phase of the input field. For example if both  $S_{j,i} \neq 0$  and  $S_{j,i+N} \neq 0$  and the input field enters the circuit from port  $i$  with average amplitude  $\langle a_i^{\text{in}} \rangle = |\langle a_i^{\text{in}} \rangle| \exp(i\varphi)$ , the intensity  $|\langle \hat{a}_j^{\text{out}} \rangle|^2$  of the field transmitted to port  $j$  depends on the phase  $\varphi$  of the input field,  $|\langle \hat{a}_j^{\text{out}} \rangle|^2 = |S_{j,i} \exp(i\varphi) + S_{j,i+N} \exp(-i\varphi)|^2 |\langle a_i^{\text{in}} \rangle|^2$ .

To simplify the discussion in the main text we have focused on phase-preserving devices. For such devices, the scattering matrix as defined in Eq. (A9a) has a block-diagonal form with two  $N \times N$  blocks mapped one into the other by the particle-hole symmetry [38]. This allows one to define the scattering matrix  $S$  as one of the two blocks obtained from Eq. (A9a) and, thus, to arrive at an  $N \times N$  matrix, consistent with Eq. (1) of the main text. In this cases, our program does not calculate the “large”  $2N \times 2N$  matrix but rather only one block.

For purely routing device (without squeezing interaction,  $\nu = 0$ ), the diagonal blocks correspond to the annihilation and creation operators, respectively. Thus, the “smaller” scattering matrix can be taken to be the block  $S_{1:N,1:N}$  of the “larger matrix” per Eq. (A8). This is also the standard definition of the scattering matrix for excitation conserving systems.

For phase-preserving amplifiers, we enforce the block structure of the “large” scattering matrix by constraining the matrix  $H$  in the following way: We divide the modes into two subsets  $M_1$  and  $M_2$  with  $N_1$  and  $N_2 = N - N_1$  modes, respectively. Then, we couple modes in the same set exclusively with beam-splitting interactions, and modes in different sets via two-mode squeezing interactions. The resulting scattering matrix has a block structure because the output fields  $a_{i \in M_1}^{\text{out}}$  and  $a_{i \in M_2}^{\text{out}\dagger}$  depend only on the input fields  $a_{i \in M_1}^{\text{in}}$  and  $a_{i \in M_2}^{\text{in}\dagger}$ , and, likewise, for the fields  $a_{i \in M_2}^{\text{out}}$ ,  $a_{i \in M_1}^{\text{out}\dagger}$ ,  $a_{i \in M_2}^{\text{in}}$ , and  $a_{i \in M_1}^{\text{in}\dagger}$ . This allows us to take as scattering matrix the block encoding the response of the output fields  $a_{i \in M_1}^{\text{out}}$  and  $a_{i \in M_2}^{\text{out}\dagger}$  to the input fields  $a_{i \in M_1}^{\text{in}}$  and  $a_{i \in M_2}^{\text{in}\dagger}$ . In practice, we calculate the “small”  $N \times N$  scattering matrix by replacing all the  $2N \times 2N$  matrices ( $\mathbb{1}_{2N}$ ,  $\sigma_z$ ,  $H$ , and  $\gamma$ ) in Eq. (A9a) with the relevant  $N \times N$  block, e.g. we replace  $\sigma_z$  with

$$\begin{pmatrix} \mathbb{1}_{N_1} & 0 \\ 0 & -\mathbb{1}_{N_2} \end{pmatrix}. \quad (\text{A11})$$

#### 4. Stability

In the presence of squeezing interactions, the Langevin equations (A3) can describe unstable motion drifting away from a saddle point. The motion is stable as long as the dynamical matrix  $D = -i\sigma_z H_{\text{BdG}} - (\kappa + \Gamma)/2$  has only eigenvalues with a negative real part.

Since the solutions obtained using our method are not necessarily stable, we exclude unstable solutions after checking their stability. We note that the eigenvalues of  $D$  as well as the signs of their real parts depend on the actual choice of  $\kappa_j$ . This can lead to constraints on these parameters.

### Appendix B: Discussion of coupling in transmission

In the main text, we have assumed that each port mode is coupled in “reflection” to the waveguide relaying the input and output signals, see Fig. S1(a). In this scenario, the port mode is coupled to a single decay channel. In this section, we discuss how to adapt our method to account for coupling in “transmission”, see Fig. S1(b).

We distinguish between two different scenarios. In the first scenario, the port mode of interest is non-chiral, e.g. a localized defect mode in a photonic crystal, see Fig. S1(c). In the second scenario, the waveguide is coupled to a pair of degenerate modes that are mapped one into the other via time-reversal and, thus, have opposite chirality, e.g. a pair of whispering gallery modes in a microresonator or a race-track resonator, see Fig. S1(d).

In the non-chiral mode scenario, the interaction of the mode with the waveguide can be modeled by introducing two decay channels, one for each propagation direction, see Fig. S1(c). In the presence of time-reversal symmetry, both decay channels have the same coupling. It is straightforward to extend our method to include port modes coupled to two input-output decay channels.

In the chiral modes scenario, the interaction region typically spans several wavelengths, and mode matching ensures that each chiral mode is coupled only with the radiation propagating in the same direction inside the waveguide. As a consequence, the interaction between each mode and the waveguide can be modeled by introducing only one decay channel, as for coupling in reflection, see Fig. S1(d). Thus, our method directly applies to this scenario.

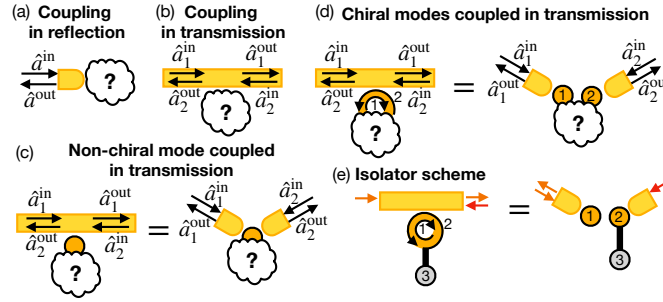


FIG. S1. (a) and (b) Sketch of two possible waveguide coupling configurations. (c) Coupling in transmission to a non-chiral mode and equivalent model with two waveguides coupled in reflection to the same mode. (d) Waveguide coupled in transmission to a racetrack resonator (or equivalent system) supporting two degenerate modes with opposite chirality (clockwise and anti-clockwise arrows) and equivalent model with two modes coupled in reflection. (e) Scheme for an isolator. Our method uses the equivalent model to rediscover the solution used in [41–44].

Special considerations are required when setting up the target scattering matrix and interpreting the couplings in the dimensionless Hamiltonian, e.g. distinguishing between passive and active coupling, see below.

### Appendix C: Application to chiral modes

Chiral modes are usually coupled in transmission to exploit their directionality. Analogously to any mode coupled in reflection, their interaction with the waveguide can be modeled using a single decay channel, see discussion in the previous section. Thus, a pair of chiral modes coupled in transmission to a waveguide (and coupled to other modes) are described by the same Langevin equations as two port modes coupled in reflection to two different waveguides (and with the same coupling to other modes). However, transmission and reflection are exchanged compared to the equivalent system with two port modes coupled in reflection. For a fixed target functionality, e.g. an isolator, the target scattering matrix should reflect this change,  $S_{ji}^{\text{target}} \leftrightarrow S_{ii}^{\text{target}}$  and  $S_{ij}^{\text{target}} \leftrightarrow S_{jj}^{\text{target}}$  with  $i$ , and  $j$  labeling the pair of chiral port modes.

As an example consider an isolator with the input fields to be injected on opposite ends of the same waveguide coupled in transmission to a pair of chiral modes. The target scattering matrix for an isolator with the two port modes coupled in reflection to the respective waveguides would be,

$$S^{\text{target}} = \begin{pmatrix} 0 & 0 \\ 1 & 0 \end{pmatrix}. \quad (\text{C1})$$

Instead, for the setup coupled in transmission we exchange transmission and reflection as described above and use the target scattering matrix

$$S^{\text{target}} = \begin{pmatrix} 1 & 0 \\ 0 & 0 \end{pmatrix}. \quad (\text{C2})$$

By using our standard method, we find that the simplest solution is a disconnected graph with a single auxiliary mode, see Fig. S1(d) right-hand side. Here, the auxiliary mode interacts only with the anti-clockwise port mode 2 with dimensionless coupling  $\tilde{g}_{23} = 1/2$  or, equivalently, cooperativity  $\mathcal{C}_{23} = 1$ . This scheme was originally proposed in [41] to implement an optical isolator using a mechanical mode as an auxiliary mode, as experimentally realized in [42–44].

We note that our classification of the scattering solutions highlighting coupling that can be implemented as passive coupling does not directly apply here. For example, considering that the port modes are mapped one onto the other via the time-reversal transformation, it follows that the coupling of an auxiliary mode to just one of them but not the other (in the isolator setup) breaks the time-reversal symmetry (irrespective of the phase of  $\tilde{g}_{23}$ ) and, thus, can not be implemented as a passive coupling. In contrast, backscattering in the racetrack resonator, which does not involve time-symmetry breaking, would be described as a complex coupling  $\tilde{g}_{12}$  between the two port modes.

### Appendix D: Effective dissipative model for the limiting case of overdamped auxiliary modes

Here, we derive the effective Markovian dissipative model obtained after integrating out a fast-decaying auxiliary mode  $\hat{a}_f$ . Such a model can be formulated in terms of a set of Langevin equations for the remaining modes or, equivalently, a Lindblad Master equation.

We assume that the dimensionless Hamiltonian  $H$  remains fixed and derive the resulting Langevin equations and the Lindbladian in terms of  $H$  and the decay rates  $\kappa_i$ . For this purpose, it is convenient to introduce the rescaled couplings  $\tilde{g}$  and  $\tilde{\nu}$ ,

$$\tilde{g} = \frac{1}{\sqrt{\kappa}} g \frac{1}{\sqrt{\kappa}}, \quad \tilde{\nu} = \frac{1}{\sqrt{\kappa}} \nu \frac{1}{\sqrt{\kappa}}. \quad (\text{D1})$$

These couplings are blocks of the rescaled Hamiltonian

$$H = \begin{pmatrix} \tilde{g} & \tilde{\nu} \\ \tilde{\nu}^* & \tilde{g}^* \end{pmatrix} \quad (\text{D2})$$

and their numerical values are directly obtained using our method. The decay rates  $\kappa_i$  can be viewed as free parameters. For simplicity, we consider the special case of a fast-decaying mode not subject to a single-mode squeezing interaction. This scenario is quite general as it applies to all phase-preserving devices as well as many phase-sensitive devices.

We start by solving the Langevin equation for the auxiliary mode.

$$\dot{\hat{a}}_f(t) = \left( i\Delta_f - \frac{\kappa_f}{2} \right) \hat{a}_f(t) - i \sum_{j \neq f} g_{fj} \hat{a}_j(t) - i \sum_{j \neq f} \nu_{fj} \hat{a}_j^\dagger(t) - \sqrt{\kappa_f} \hat{a}_f^{\text{in}}(t) \quad (\text{D3})$$

to find

$$\hat{a}_f(t) = - \int_{-\infty}^t dt' e^{(i\Delta_f - \kappa_f/2)(t-t')} \left( i \sum_{j \neq f} g_{fj} \hat{a}_j(t') + i \sum_{j \neq f} \nu_{fj} \hat{a}_j^\dagger(t') + \sqrt{\kappa_f} \hat{a}_f^{\text{in}}(t') \right). \quad (\text{D4})$$

In the limit  $\kappa_f/\kappa_i \rightarrow \infty$  we can set  $\hat{a}_j(t') = \hat{a}_j(t)$ ,  $\hat{a}_j^\dagger(t') = \hat{a}_j^\dagger(t)$ , and  $\hat{a}_f^{\text{in}}(t') = \hat{a}_f^{\text{in}}(t)$  into the integral. With this Markovian approximation, we can calculate the integral explicitly

$$\hat{a}_f(t) = \frac{1}{i\Delta_f - \kappa_f/2} \left( i \sum_{j \neq f} g_{fj} \hat{a}_j(t) + i \sum_{j \neq f} \nu_{fj} \hat{a}_j^\dagger(t) + \sqrt{\kappa_f} \hat{a}_f^{\text{in}}(t) \right) \quad (\text{D5a})$$

$$= - \frac{2}{\kappa_f} \frac{1 + 2i\Delta_f/\kappa_f}{1 + 4(\Delta_f/\kappa_f)^2} \left( i \sum_{j \neq f} g_{fj} \hat{a}_j(t) + i \sum_{j \neq f} \nu_{fj} \hat{a}_j^\dagger(t) + \sqrt{\kappa_f} \hat{a}_f^{\text{in}}(t) \right). \quad (\text{D5b})$$

By plugging Eq. (D5) into the input-output relation

$$\hat{a}_f^{\text{out}} = \hat{a}_f^{\text{in}} + \sqrt{\kappa_f} \hat{a}_f. \quad (\text{D6})$$

and expressing in terms of  $\tilde{g}_{fk}$  and  $\tilde{\nu}_{fk}$  we find

$$\hat{a}_f^{\text{out}} = -e^{2i\varphi_f} \hat{a}_f^{\text{in}} - 2i \frac{\exp(i\varphi_f)}{\sqrt{1 + 4\tilde{g}_{ff}^2}} \sum_{k \neq f} \sqrt{\kappa_k} \left( \tilde{g}_{fk} \hat{a}_k + \tilde{\nu}_{fk} \hat{a}_k^\dagger \right), \quad (\text{D7})$$

with  $\varphi_f = \arg(1 - 2i\tilde{g}_{ff})$ . It is convenient to apply a gauge transformation to the input field,  $\hat{a}_f^{\text{in}} = -e^{2i\varphi_f} \hat{a}_f^{\text{in}}$  and define the Bogoliubov operator

$$\hat{z} = \sum_{k \neq f} c_k^- \hat{a}_k + c_k^+ \hat{a}_k^\dagger, \quad [\hat{z}, \hat{z}^\dagger] = \text{sgn}(\mathcal{N}_z) \quad (\text{D8})$$

with

$$c_k^- = -ie^{i\varphi_f} \sqrt{\frac{\kappa_k}{|\mathcal{N}_z|}} \tilde{g}_{fk}, \quad c_k^+ = -ie^{i\varphi_f} \sqrt{\frac{\kappa_k}{|\mathcal{N}_z|}} \tilde{\nu}_{fk}, \quad \mathcal{N}_z = \sum_{j \neq f} \kappa_j (|\tilde{g}_{fj}|^2 - |\tilde{\nu}_{fj}|^2). \quad (\text{D9})$$

We note that  $\hat{z}$  is an annihilation (creation) operator for  $\mathcal{N}_z > 0$  ( $\mathcal{N}_z < 0$ ). The above definitions allow one to rewrite the input-output relations as

$$\hat{a}_f^{\text{out}} = \hat{a}_f^{\text{in}} + \sqrt{\Gamma^{\text{eff}}}\hat{z}, \quad (\text{D10})$$

with

$$\Gamma^{\text{eff}} = \frac{4|\mathcal{N}_z|}{1 + 4\tilde{g}_{ff}^2}. \quad (\text{D11})$$

We anticipate that  $\hat{z}$  can be interpreted as a jump operator and  $\Gamma^{\text{eff}}$  as the corresponding dissipative rate. More precisely, the dissipative dynamics is described by the Lindblad master Equation

$$\dot{\hat{\rho}} = -i[\hat{H}^{\text{eff}}, \hat{\rho}] + \sum_{i \neq f} \kappa_i \mathcal{L}[\hat{a}_i](\hat{\rho}) + \Gamma^{\text{eff}} \mathcal{L}[\hat{z}](\hat{\rho}). \quad (\text{D12})$$

where  $\hat{\rho}$  is the density matrix,  $\hat{H}^{\text{eff}}$  an effective second-quantized Hamiltonian in the form,

$$\hat{H}^{\text{eff}} = \frac{1}{2} \sum_{j, k \neq f} \left( g_{jk}^{\text{eff}} \hat{a}_j^\dagger \hat{a}_k + \nu_{jk}^{\text{eff}} \hat{a}_j^\dagger \hat{a}_k^\dagger \right) + \text{H.c.}, \quad (\text{D13})$$

and  $\mathcal{L}[\hat{A}]$  is the Lindblad superoperator,

$$\mathcal{L}[\hat{A}](\hat{\rho}) = \hat{A}\hat{\rho}\hat{A}^\dagger - \frac{1}{2}\hat{\rho}\hat{A}^\dagger\hat{A} - \frac{1}{2}\hat{A}^\dagger\hat{A}\hat{\rho}. \quad (\text{D14})$$

We note that for  $\mathcal{N}_z > 0$  ( $\mathcal{N}_z < 0$ ) the collective Bogoliubov excitations decay (are absorbed) into (from) the effective Markovian bath. We note that Eq. (D12) does not depend on  $\mathcal{N}_z$ , cf Eqs. (D9) and Eq. (D11). Thus, it is still well defined in the special limiting case  $\mathcal{N}_z = 0$  even though Eq. (D9) is not. In this case, the jump operator  $\hat{z}$  can not be chosen to be a Bogoliubov operator. An alternative choice is to choose it to be a multimode quadrature

$$\hat{z} = \sum_{k \neq f} c_k^- \hat{a}_k + c_k^+ \hat{a}_k^\dagger, \quad \hat{p} = i \sum_{k \neq f} c_k^- \hat{a}_k^\dagger - c_k^+ \hat{a}_k, \quad [\hat{z}, \hat{p}] = i, \quad (\text{D15})$$

with

$$c_k^- = -ie^{i\varphi_f} \sqrt{\frac{\kappa_k}{|\mathcal{N}_z|}} \tilde{g}_{fk}, \quad c_k^+ = -ie^{i\varphi_f} \sqrt{\frac{\kappa_k}{|\mathcal{N}_z|}} \tilde{\nu}_{fk}, \quad \mathcal{N}_z = \sum_{j \neq f} \kappa_j (|\tilde{g}_{fj}|^2 + |\tilde{\nu}_{fj}|^2). \quad (\text{D16})$$

To further substantiate our interpretations of  $\hat{z}$  and  $\Gamma^{\text{eff}}$  we plug Eq. (D5) into the Langevin equations for the remaining modes

$$\dot{\hat{a}}_j(t) = -i \sum_k g_{jk} \hat{a}_k(t) - i \sum_k \nu_{jk} \hat{a}_k^\dagger(t) - \frac{\kappa_j + \Gamma_j}{2} \hat{a}_j(t) - \sqrt{\kappa_j} \hat{a}_j^{\text{in}}(t) - \sqrt{\Gamma_j} \hat{a}_j^{\text{noise}}(t) \quad (\text{D17})$$

to find the effective Langevin equation

$$\begin{aligned} \dot{\hat{a}}_j(t) = & - \sum_{k \neq f} [(c_j^- c_k^- - c_j^+ c_k^+) \Gamma^{\text{eff}} / 2 + i g_{jk}^{\text{eff}}] \hat{a}_k(t) - \sum_{k \neq f} [(c_j^- c_k^+ - c_j^+ c_k^-) \Gamma^{\text{eff}} / 2 + i \nu_{jk}^{\text{eff}}] \hat{a}_k^\dagger(t) \\ & - \frac{\kappa_j + \Gamma_j}{2} \hat{a}_j(t) - \sqrt{\kappa_j} \hat{a}_j^{\text{in}}(t) - \sqrt{\Gamma_j} \hat{a}_j^{\text{noise}}(t) - \sqrt{\Gamma^{\text{eff}}} c_j^- \hat{a}_f^{\text{in}}(t) - \sqrt{\Gamma^{\text{eff}}} c_j^+ \hat{a}_f^{\text{in}\dagger}(t), \end{aligned} \quad (\text{D18})$$

with the effective coherent couplings

$$g_{jk}^{\text{eff}} = g_{jk} - \sqrt{\kappa_j \kappa_k} \frac{4\tilde{g}_{ff}}{1 + 4\tilde{g}_{ff}^2} (\tilde{g}_{jf} \tilde{g}_{fk} + \tilde{\nu}_{jf} \tilde{\nu}_{fk}^*) \quad (\text{D19})$$

$$\nu_{jk}^{\text{eff}} = g_{jk} - \sqrt{\kappa_j \kappa_k} \frac{4\tilde{g}_{ff}}{1 + 4\tilde{g}_{ff}^2} (\tilde{g}_{jf} \tilde{\nu}_{fk} + \tilde{\nu}_{jf} \tilde{g}_{fk}^*). \quad (\text{D20})$$

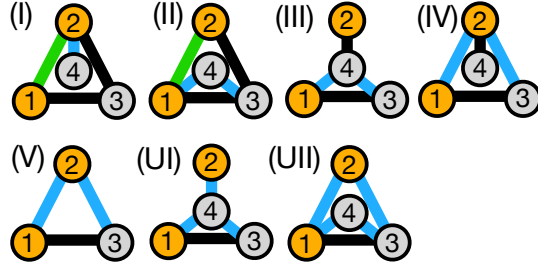


FIG. S2. All irreducible graphs identified for the fully-directional phase preserving quantum-limited amplifier. Mode 1 is the input mode, mode 2 the output. Graph (I-V) have a stable parameter regime. For graph (VI) and (VII) we did not identify a stable regime.

The terms proportional to the decay rate  $\Gamma^{\text{eff}}$  describe dissipative interactions. By comparing the corresponding equations for the mean fields  $\langle \hat{a}_i \rangle$  and those straightforwardly calculated from the Lindblad master Eq. (D12), one can verify that the two sets of equations are identical and, thus, confirm our interpretation of  $\hat{z}$  and  $\Gamma^{\text{eff}}$ .

To illustrate our general method we apply it to some specific examples of interest. The simplest possible scenario features a resonant fast-decaying auxiliary mode ( $\tilde{g}_{ff} = 0$ ) coupled to a single port mode  $j$  with a beamsplitter interaction, see e.g. the setups (IV) in Fig. S2. Applying Eqs. (D8-D11) we find  $\hat{z} = -i\tilde{g}_{ffj}/|\tilde{g}_{ffj}\hat{a}_j$  and  $\Gamma^{\text{eff}} = 4\kappa_j|\tilde{g}_{ffj}|^2 = 4|g_{ffj}|^2/\kappa_f$ . Thus, the auxiliary mode can be replaced with a simple loss channel recovering the solution corresponding to graph (V) in Fig. S2. If the fast-decaying mode and the port mode are coupled via a pair-creation interaction, as in the setups (I) in Fig. S2, the auxiliary mode can be replaced by a gain channel corresponding to  $\hat{z} = -i\tilde{\nu}_{ffj}/|\tilde{\nu}_{ffj}\hat{a}_j^\dagger$  and  $\Gamma^{\text{eff}} = 4\kappa_j|\tilde{\nu}_{ffj}|^2 = 4|\nu_{ffj}|^2/\kappa_f$ .

Next, we consider the setups discussed in [35] with a resonant fast-decaying auxiliary mode coupled to two port modes. If the modes are coupled pairwise via passive and nonreciprocal couplings to realize an isolator [see Fig. 3(a) of the main text] the matrix elements of the dimensionless Hamiltonian obtained using our method read  $\tilde{g}_{12} = i/2$ ,  $\tilde{g}_{23} = 1/2$ , and  $\tilde{g}_{31} = 1/2$ . Applying Eqs. (D8-D11) we find

$$\hat{z} = -\frac{i}{\sqrt{\kappa_1 + \kappa_2}}(\sqrt{\kappa_1}\hat{a}_1 + \sqrt{\kappa_2}\hat{a}_2), \quad \Gamma^{\text{eff}} = \kappa_1 + \kappa_2.$$

This is the same solution derived in [35] for the special case  $\kappa_1 = \kappa_2$ .

One can also operate the same three modes setup as a quantum-limited amplifier. Using our method we recover the same solution also used in [2, 34–38]. The required dimensionless matrix elements read  $\tilde{\nu}_{12} = \tilde{\nu}_{21} = iF(G)/2$ ,  $\tilde{\nu}_{23} = \tilde{\nu}_{32} = F(G)/2$ , and  $\tilde{g}_{31} = \tilde{g}_{13} = 1/2$  with  $F(G) = \sqrt{G-1}/(1+\sqrt{G})$  (all other matrix elements are zero). As in [35] we consider  $\kappa_1 = \kappa_2$  which corresponds to a stable system. Applying Eqs. (D8-D11) we find

$$\hat{z} = -\frac{i}{\sqrt{1-F^2(G)}}(\hat{a}_1 + F(G)\hat{a}_2^\dagger), \quad \Gamma^{\text{eff}} = \kappa_1(1-F^2(G)),$$

recovering the same dissipative scheme as in [35].

### Appendix E: Fully-directional phase-preserving quantum-limited amplifier

Here, we give more details on all irreducible-graph solutions for the fully directional phase-preserving quantum-limited amplifier, see Fig. 3(c). In Fig. S2, we display all discovered graphs, here, including also those for which we did not find a stable parameter regime.

The analytical expressions for the scattering matrix  $S(G)$  given below are inferred by analytical regression starting from a dataset of solutions created by applying our method for a set of  $G$  values. The corresponding analytical expressions for the dimensionless Bogoliubov Hamiltonian  $H(G)$  are then obtained by solving Eq. (A9a).

### 1. Graph I

The scattering matrix for Graph (I) reads

$$S = \begin{pmatrix} 0 & 0 & -i & 0 \\ \sqrt{G} & 0 & 0 & i\sqrt{G-1}e^{i\varphi_{24}} \\ i(G-1) & -i\sqrt{G} & 0 & -\sqrt{G}\sqrt{G-1}e^{i\varphi_{24}} \\ i\sqrt{G}\sqrt{G-1}e^{-i\varphi_{24}} & -i\sqrt{G-1}e^{-i\varphi_{24}} & 0 & -G \end{pmatrix}. \quad (\text{E1})$$

The underlying matrix elements of the dimensionless Hamiltonian read  $g_{12}/\sqrt{\kappa_1\kappa_2} = i\sqrt{G}/2$ ,  $g_{13}/\sqrt{\kappa_1\kappa_3} = -1/2$ ,  $g_{23}/\sqrt{\kappa_2\kappa_3} = -\sqrt{G}/2$ , and  $\nu_{24}/\sqrt{\kappa_2\kappa_4} = \sqrt{G-1}e^{i\varphi_{24}}/2$ . We note that the phase  $\varphi_{24} \equiv \arg \nu_{24}$  can be fixed to any arbitrary value. In this solution, the phase acquired from the input mode 1 to the output mode 2 assumes the value  $\pi/2$  while the remaining coupling amplitudes are real, corresponding to an overall flux  $\Phi_{123} = \pi/2$ . We note that the free phases  $\gamma_j^{\text{out/in}}$  in the cost function allow one to arbitrarily change the coupling phases and still find a valid solution as long as the flux  $\Phi_{123}$  remains the same. In this way, one can change the number of green edges or arrive at a different valid irreducible graph with a single green edge connecting sites 1 and 3 or 2 and 3. We view all these solutions as equivalent. We have checked that for  $\kappa_1 = \kappa_2 = \kappa_3 = \kappa_4$  the system is stable for all values of  $G$ .

### 2. Graph II

The scattering matrix for Graph (II) reads

$$S = \begin{pmatrix} 0 & 0 & -i & 0 \\ \sqrt{G} & 0 & 0 & -i\sqrt{G-1}e^{i\varphi_{14}} \\ i(1-G) & -i\sqrt{G} & 0 & -\sqrt{G}\sqrt{G-1}e^{i\varphi_{14}} \\ -i\sqrt{G}\sqrt{G-1}e^{-i\varphi_{14}} & -i\sqrt{G-1}e^{-i\varphi_{14}} & 0 & -G \end{pmatrix}. \quad (\text{E2})$$

The underlying matrix elements of the dimensionless Hamiltonian read  $g_{12}/\sqrt{\kappa_1\kappa_2} = i/(2\sqrt{G})$ ,  $g_{13}/\sqrt{\kappa_1\kappa_3} = -1/2$ ,  $\nu_{14}/\sqrt{\kappa_1\kappa_4} = \sqrt{G-1}e^{i\varphi_{14}}/(2\sqrt{G})$ ,  $g_{23}/\sqrt{\kappa_2\kappa_3} = -1/(2\sqrt{G})$ ,  $\nu_{34}/\sqrt{\kappa_3\kappa_4} = i\sqrt{G-1}e^{i\varphi_{14}}/(2\sqrt{G})$ . Here, the phase  $\varphi_{14} \equiv \arg \nu_{14}$  is a free parameter. Equivalent irreducible graphs have a single green edge connecting modes 1 and 3 or 2 and 3. We have checked that for  $\kappa_1 = \kappa_2 = \kappa_3 = \kappa_4$ , the system is stable for all values of  $G$ .

### 3. Graph III

The scattering matrix for Graph (III) reads

$$S = \begin{pmatrix} 0 & 0 & -i & 0 \\ -\sqrt{G}e^{-i\varphi_{14}} & 0 & 0 & i\sqrt{G+1} \\ i(-G-1) & i\sqrt{G}e^{i\varphi_{14}} & 0 & -\sqrt{G}\sqrt{G+1}e^{i\varphi_{14}} \\ -i\sqrt{G}\sqrt{G+1}e^{-i\varphi_{14}} & i\sqrt{G+1} & 0 & -G \end{pmatrix}. \quad (\text{E3})$$

The underlying matrix elements of the dimensionless Hamiltonian read  $g_{13}/\sqrt{\kappa_1\kappa_3} = -1/2$ ,  $\nu_{14}/\sqrt{\kappa_1\kappa_4} = \sqrt{G}e^{i\varphi_{14}}/(2\sqrt{G+1})$ ,  $g_{24}/\sqrt{\kappa_2\kappa_4} = -1/(2\sqrt{G+1})$ ,  $\nu_{34}/\sqrt{\kappa_3\kappa_4} = i\sqrt{G}e^{i\varphi_{14}}/(2\sqrt{G+1})$ . The phase  $\varphi_{14} \equiv \arg \nu_{14}$  is a free parameter. We have checked that for  $\kappa_1 = \kappa_2 = \kappa_3 = \kappa_4$  the system is stable for all values of  $G$ .

### 4. Graph IV

The scattering matrix for Graph (IV) reads

$$S = \begin{pmatrix} 0 & 0 & -i & 0 \\ -i\sqrt{G}e^{-i\varphi_{12}} & 0 & 0 & i\sqrt{G+1} \\ i(-G-1) & -\sqrt{G}e^{i\varphi_{12}} & 0 & i\sqrt{G}\sqrt{G+1}e^{i\varphi_{12}} \\ -\sqrt{G}\sqrt{G+1}e^{-i\varphi_{12}} & i\sqrt{G+1} & 0 & G \end{pmatrix}. \quad (\text{E4})$$

The underlying matrix elements of the dimensionless Hamiltonian read  $\nu_{12}/\sqrt{\kappa_1\kappa_2} = \sqrt{G}e^{i\varphi_{12}}/2$ ,  $g_{13}/\sqrt{\kappa_1\kappa_3} = -1/2$ ,  $\nu_{23}/\sqrt{\kappa_2\kappa_3} = i\sqrt{G}e^{i\varphi_{12}}/2$ ,  $g_{24}/\sqrt{\kappa_2\kappa_4} = -\sqrt{G+1}/2$  with the free parameter  $\varphi_{12}$ . We have checked that for  $\kappa_1 = \kappa_2 = \kappa_3$  and  $\kappa_4/\kappa_1 = G$  the system is stable for all values of  $G$ .

### 5. Graph V

The scattering matrix for Graph (V) reads

$$S = \begin{pmatrix} 0 & 0 & -i \\ -i\sqrt{G}e^{-i\varphi_{12}} & 0 & 0 \\ i(-G-1) & -\sqrt{G}e^{i\varphi_{12}} & 0 \end{pmatrix}. \quad (\text{E5})$$

The underlying matrix elements of the dimensionless Hamiltonian read  $\nu_{12}/\sqrt{\kappa_1\kappa_2} = \sqrt{G}e^{i\varphi_{12}}/2$ ,  $g_{13}/\sqrt{\kappa_1\kappa_3} = -1/2$  and  $\nu_{23}/\sqrt{\kappa_2\kappa_3} = i\sqrt{G}e^{i\varphi_{12}}/2$ . In addition, the intrinsic loss rate of the output mode is  $\Gamma_2/\kappa_2 = G+1$ . The phase  $\varphi_{12}$  is a free parameter. We have checked that for  $\kappa_1 = \kappa_2 = \kappa_3$  the system is stable for all values of  $G$ .

As mentioned above solution (V) can be recovered starting from solution (IV) by applying our general method outlined in the Supplementary Section D to integrate out the auxiliary mode 4.

### 6. Graph UI

The scattering matrix for Graph (UI) reads

$$S = \begin{pmatrix} 0 & 0 & i & 0 \\ \sqrt{G}e^{-i(\varphi_{14}-\varphi_{24})} & 0 & 0 & -i\sqrt{G-1}e^{i\varphi_{24}} \\ i(1-G) & -i\sqrt{G}e^{i(\varphi_{14}-\varphi_{24})} & 0 & -\sqrt{G}\sqrt{G-1}e^{i\varphi_{14}} \\ i\sqrt{G}\sqrt{G-1}e^{-i\varphi_{14}} & i\sqrt{G-1}e^{-i\varphi_{24}} & 0 & G \end{pmatrix}. \quad (\text{E6})$$

The underlying matrix elements of the dimensionless Hamiltonian read  $g_{13}/\sqrt{\kappa_1\kappa_3} = 1/2$ ,  $\nu_{14}/\sqrt{\kappa_1\kappa_4} = \sqrt{G}e^{i\varphi_{14}}/(2\sqrt{G-1})$ ,  $\nu_{24}/\sqrt{\kappa_2\kappa_4} = e^{i\varphi_{24}}/(2\sqrt{G-1})$ ,  $\nu_{34}/\sqrt{\kappa_3\kappa_4} = -i\sqrt{G}e^{i\varphi_{14}}/(2\sqrt{G-1})$ .  $\varphi_{14}$  and  $\varphi_{24}$  are coupling phases and can be chosen arbitrarily. We did not identify any stable parameter regime for this graph.

### 7. Graph UII

The scattering matrix for Graph (UII) reads

$$S = \begin{pmatrix} 0 & 0 & -i & 0 \\ -i\sqrt{G} & 0 & 0 & \sqrt{G+1} \\ i(G+1) & -\sqrt{G} & 0 & -\sqrt{G^2+G} \\ -i\sqrt{G^2+G} & \sqrt{G+1} & 0 & G \end{pmatrix}. \quad (\text{E7})$$

The underlying matrix elements of the dimensionless Hamiltonian read  $\nu_{12}/\sqrt{\kappa_1\kappa_2} = -1/(2\sqrt{G})$ ,  $g_{13}/\sqrt{\kappa_1\kappa_3} = -1/2$ ,  $\nu_{14}/\sqrt{\kappa_1\kappa_4} = -\sqrt{G+1}/(2\sqrt{G})$ ,  $\nu_{23}/\sqrt{\kappa_2\kappa_3} = -i/(2\sqrt{G})$ , and  $\nu_{34}/\sqrt{\kappa_3\kappa_4} = -i\sqrt{G+1}/(2\sqrt{G})$ . We chose the coupling phases of  $\varphi_{12}$  and  $\varphi_{14}$  to be  $\pi$ . As long as the sum of phases of each loop is conserved, the phases of all the parametric couplings can be set to any value. We were not able to identify any stable parameter regime for this graph.

### 8. Noise analysis

The field operators for the input and noise channels  $\hat{a}_j^{\text{in}}$  and  $\hat{a}_j^{\text{noise}}$  obey the correlators:

$$\langle \hat{a}_j^{\dagger,\text{in}}(t)\hat{a}_j^{\text{in}}(t') \rangle = n_j^{\text{in}}\delta(t-t') \quad (\text{E8a})$$

$$\langle \hat{a}_j^{\text{in}}(t)\hat{a}_j^{\dagger,\text{in}}(t') \rangle = (n_j^{\text{in}}+1)\delta(t-t') \quad (\text{E8b})$$

$$\langle \hat{a}_j^{\dagger,\text{noise}}(t)\hat{a}_j^{\text{noise}}(t') \rangle = n_j^{\text{noise}}\delta(t-t') \quad (\text{E8c})$$

$$\langle \hat{a}_j^{\text{noise}}(t)\hat{a}_j^{\dagger,\text{noise}}(t') \rangle = (n_j^{\text{noise}}+1)\delta(t-t') \quad (\text{E8d})$$



with  $n_j^{\text{in}}$  and  $n_j^{\text{noise}}$  as the occupation number of the baths connected to the respective mode.

The number of added noise photons on the input (mode 1) and output channel (mode 2) equals:

$$N_{\text{input}}^{\text{add}} = \frac{1}{2} \sum_k \left( (n_k^{\text{in}} + 1) |S_{1k}|^2 + (n_k^{\text{noise}} + 1) |N_{1k}|^2 \right) \quad (\text{E9a})$$

$$N_{\text{output}}^{\text{add}} = \frac{1}{2} \sum_{k \neq 1} \left( (n_k^{\text{in}} + 1) |S_{2k}|^2 + (n_k^{\text{noise}} + 1) |N_{2k}|^2 \right) \quad (\text{E9b})$$

The quantum limit for a phase-preserving amplifiers is  $N_{\text{input}}^{\text{add}} = 1/2$  and  $N_{\text{output}}^{\text{add}} = (G-1)/2$  [39]. We assume that all the baths are at zero temperature, except the bath connected to the output channel. So,  $n_j^{\text{in}} = 0$  if  $j \neq 2$ ,  $n_j^{\text{noise}} = 0$  for all  $j$ , and  $n_2^{\text{in}} > 0$ .

During optimization, we set  $N_{\text{input}}^{\text{add}} = 1/2$  as an additional constraint during the optimization. Therefore, all identified architectures fulfill this equality constraint. The quantum limit for the output channel was not as additional constraint and is analysed in the following.

For Graph (I,II,UI) the number of added photons on the output channel turn out to equal  $N_{\text{output}}^{\text{add}} = (G-1)/2$ , therefore, reaching the quantum limit for all  $G$ . For the graphs (III-V,UII)  $N_{\text{output}}^{\text{add}} = (G+1)/2$ . So, the number of added photons is close to the quantum limit and approaches it in the limit of  $G \rightarrow \infty$ .

## Appendix F: Bus modes

Here, we give more details on how we have augmented our standard method to treat the bus modes in optomechanical and other hybrid systems that feature constraints in the connectivity of the port modes. These modifications are introduced to facilitate the discovery of schemes that require infinite cooperativity between the bus modes and other modes to reach the ideal behavior.

### 1. Far-detuned bus modes

To discover schemes in which one or more bus modes mediate purely coherent interactions between the port modes we introduce as an additional building block of our discrete optimization a far-detuned bus mode. Formally, we set the decay rates of this type of mode to zero and at the same time assume that their detuning is not zero. This allows us to eliminate all far-detuned modes and incorporate their effect into an effective Hamiltonian for the remaining modes, as shown below.

For  $N$  standard modes  $\hat{a}_j$  and  $M$  far-detuned modes  $\hat{b}_j$  the most general quadratic Hamiltonian reads:

$$\hat{H} = \frac{1}{2} \sum_{jk=1}^{NN} \left( g_{jk}^{(aa)} \hat{a}_j^\dagger \hat{a}_k + \nu_{jk}^{(aa)} \hat{a}_j^\dagger \hat{a}_k^\dagger \right) + \frac{1}{2} \sum_{jk=1}^{MM} \left( g_{jk}^{(bb)} \hat{b}_j^\dagger \hat{b}_k + \nu_{jk}^{(bb)} \hat{b}_j^\dagger \hat{b}_k^\dagger \right) + \sum_{jk=1}^{NM} \left( g_{jk}^{(ab)} \hat{a}_j^\dagger \hat{b}_k + \nu_{jk}^{(ab)} \hat{a}_j^\dagger \hat{b}_k^\dagger \right) + \text{H.c.}, \quad (\text{F1})$$

where  $g^{(aa)}$  and  $g^{(bb)}$  are hermitian matrices,  $\nu^{(aa)}$  and  $\nu^{(bb)}$  are symmetric matrices, and  $g^{(ab)}$  and  $\nu^{(ab)}$  are arbitrary matrices. To compactly rewriting the effective Hamiltonian, it is convenient to define the matrices

$$H_{\text{BdG}}^{(ss')} = \begin{pmatrix} g^{(ss')} & \nu^{(ss')} \\ \nu^{(ss')*} & g^{(ss')*} \end{pmatrix} \quad (\text{F2})$$

with  $s, s' = a$  or  $b$  and  $g^{(ba)} = g^{(ab)*}$  and  $\nu^{(ba)} = \nu^{(ab)}$ . These matrices can be viewed as blocks of the underlying Bogoliubov de Gennes Hamiltonian. The effective Bogoliubov de Gennes Hamiltonian can be written as

$$H_{\text{BdG}}^{(\text{eff})} = H_{\text{BdG}}^{(\text{aa})} - H_{\text{BdG}}^{(\text{ab})} (H_{\text{BdG}}^{(\text{bb})})^{-1} H_{\text{BdG}}^{(\text{ba})}. \quad (\text{F3})$$

The corresponding second-quantized Hamiltonian reads

$$\hat{H} = \frac{1}{2} \sum_{jk=1}^{NN} \left( g_{jk}^{(\text{eff})} \hat{a}_j^\dagger \hat{a}_k + \nu_{jk}^{(\text{eff})} \hat{a}_j^\dagger \hat{a}_k^\dagger \right) + \text{H.c.} \quad (\text{F4})$$

with

$$H_{\text{BdG}}^{(\text{eff})} = \begin{pmatrix} g^{(\text{eff})} & \nu^{(\text{eff})} \\ \nu^{(\text{eff})*} & g^{(\text{eff})*} \end{pmatrix} \quad (\text{F5})$$

Next, we assume that the Bogoliubov de Gennes Hamiltonian  $H_{\text{BdG}}^{(bb)}$  projected on the far-detuned modes had been diagonalized to eliminate any coupling between the bus modes. In other words,  $\nu^{(bb)}$  is zero and  $g^{(bb)}$  is diagonal with  $g_{ii}^{(bb)} = -\Delta_i^{(b)}$ . In this case, we find

$$g_{ij}^{(\text{eff})} = g_{ij}^{(aa)} + \sum_k \frac{g_{ik}^{(ab)} g_{kj}^{(ab)*}}{\Delta_k^{(b)}} + \frac{\nu_{ik}^{(ab)} \nu_{kj}^{(ab)*}}{\Delta_k^{(b)}} \quad (\text{F6})$$

$$\nu_{ij}^{(\text{eff})} = \nu_{ij}^{(aa)} + \sum_k \frac{g_{ik}^{(ab)} \nu_{kj}^{(ab)}}{\Delta_k^{(b)}} + \frac{\nu_{ik}^{(ab)} g_{kj}^{(ab)}}{\Delta_k^{(b)}}. \quad (\text{F7})$$

Thus, the rescaled Bogoliubov Hamiltonian in Eq. (A9a) is modified as following

$$H_{ij} = \frac{g_{ij}^{(aa)}}{\sqrt{\kappa_i \kappa_j}} + \sum_k \text{sgn}(\Delta_k) \left( \frac{g_{ik}^{(ab)}}{\sqrt{\kappa_i |\Delta_k^{(b)}|}} \frac{g_{kj}^{(ab)*}}{\sqrt{\kappa_j |\Delta_k^{(b)}|}} + \frac{\nu_{ik}^{(ab)}}{\sqrt{\kappa_i |\Delta_k^{(b)}|}} \frac{\nu_{kj}^{(ab)*}}{\sqrt{\kappa_j |\Delta_k^{(b)}|}} \right). \quad (\text{F8})$$

or

$$H_{ij} = \frac{\nu_{ij}^{(aa)}}{\sqrt{\kappa_i \kappa_j}} + \sum_k \text{sgn}(\Delta_k) \left( \frac{g_{ik}^{(ab)}}{\sqrt{\kappa_i |\Delta_k^{(b)}|}} \frac{\nu_{kj}^{(ab)}}{\sqrt{\kappa_j |\Delta_k^{(b)}|}} + \frac{\nu_{ik}^{(ab)}}{\sqrt{\kappa_i |\Delta_k^{(b)}|}} \frac{g_{kj}^{(ab)}}{\sqrt{\kappa_j |\Delta_k^{(b)}|}} \right). \quad (\text{F9})$$

We use the dimensionless parameters and  $g_{ik}^{(ab)}/\sqrt{\kappa_i \Delta_k^{(b)}}$  with  $k = 1, \dots, M$  and  $i = 1, \dots, N$  as additional learning parameters of our continuous optimization. The signs  $\text{sgn}(\Delta_k)$  remain fixed during the continuous optimization and are, instead, chosen within the discrete optimization. Note the different scaling of the learning parameters encoding the interaction with a bus mode with the detuning  $\Delta_k^{(b)}$  playing the role of the decay rate  $\kappa_k^{(b)}$ . This scaling reflects that the coherent interactions mediated by the bus modes become independent of the bus mode decay  $\kappa_k^{(b)}$  in the asymptotic limit of large cooperativities,  $4|g_{ik}^{(ab)}|^2/|\kappa_i \kappa_k^{(b)}| \rightarrow \infty$ . Similar to the decay rates  $\kappa_i$  of the standard modes, we can view the detunings  $\Delta_i^{(b)}$  of the far-detuned bus mode as free parameters (possibly subject to some stability constraints).